3D analysis from micro-MRI during *in situ* compression on cancellous bone

Aurélie Benoit [a], Sandra Guérard [a,*], Brigitte Gillet [b], Geneviève Guillot [c], François Hild [d], David Mitton [a], Jean-Noël Périé [d,1], Stéphane Roux [d]

[a] *Arts et Metiers ParisTech, CNRS, LBM, 151 bd de l'Hopital, 75013 Paris, France*
[b] *Laboratoire de RMN biologique, ICSN CNRS UPR 2301, 1 Avenue de la Terrasse, 91198 Gif sur Yvette, France*
[c] *U2R2M UMR8081 CNRS-Univ Paris-Sud, Bât 220, 91405 Orsay, France*
[d] *LMT-Cachan, ENS Cachan/CNRS/UPMC/PRES UniverSud Paris, 61 Avenue du Président Wilson, F-94235 Cachan Cedex, France*

Keywords:
3D digital image correlation
Mechanical characterization
Cancellous bone

A B S T R A C T

A mini-compression jig was built to perform *in situ* tests on bovine trabecular bone monitored by micro-MRI. The MRI antenna provided an isotropic resolution of 78 μm that allows for a volume correlation method to be used. Three-dimensional displacement fields are then evaluated within the bone sample during the compression test. The performances of the correlation method are evaluated and discussed to validate the technique on trabecular bone. By considering correlation residuals and estimates of acquisition noise, the measured results are shown to be trustworthy. By analyzing average strain levels for different interrogation volumes along the loading direction, it is shown that the sample size is less than that of a representative volume element. This study shows the feasibility of the 3D-displacement and strain field analyses from micro-MRI images. Other biological tissues could be considered in future work.

1. Introduction

Mechanical properties of cancellous bone have been investigated for many years using different methods and it has been proven that they depend upon their apparent density (Carter and Hayes, 1976; Rice et al., 1988). Moreover, the contribution of the microstructure to the mechanical properties is widely accepted (Mosekilde, 1988; Parfitt, 1987). In order to take into account these different parameters, finite-element models of cancellous bone specimens have been proposed (Hollister et al., 1994; van Rietbergen et al., 1995). Model validations are often based on global measurements. Local measurements thanks to the digital image correlation (DIC) that is based on textured surfaces were used to measure local strains with cortical bone images (Duchemin et al., 2008; Liu and Morgan, 2007; Nicolella et al., 2001). This technique was also developed in 3D and applied to bone (Bay et al., 1999; Nazarian and Muller, 2004) or to solid foam to estimate 3D-displacement fields (Verhulp et al., 2004; Roux et al., 2008). Such data are extremely useful in particular for extensive finite-element model validation (Zauel et al., 2006). Moreover 3D-displacement fields may also be used to determine material properties.

We propose in this study to apply such measurement technique on cancellous bone by using a nonirradiating imaging method such as micro-MRI. The resolution can be less than the trabecular thickness so that the trabecular network is used as a random texture for the correlation technique. Moreover, micro-MRI limits temperature rise within the tested specimen and allows for future (similar) works on ligaments, muscles or cartilage.

Displacement mapping at subvoxel accuracy in soft tissues (e.g., muscle, cartilage) has been already demonstrated by different MR techniques (Neu and Walton, 2008). Among these, MR elastography directly maps the shear stiffness in different tissues by visualizing the propagation velocity of shear waves (Glaser et al., 2006). However such approaches would fail with trabecular bone, due to the complexity of the bone marrow interface, namely, local field heterogeneities due to magnetic susceptibility mismatch would make phase encoding displacement unreliable, and shear wave propagation would not be exploitable due to the strong difference in mechanical response between the stiff matrix and the soft marrow. For these reasons, we resorted to a direct method to obtain 3D-displacement fields in trabecular bone.

In the present study, a 3D 'finite-element based' digital image correlation method is used to determine displacement and strain fields of trabecular bone based on the real microstructure imaged

* Corresponding author. Fax: +33 1 44 24 63 66.
E-mail address: sandra.guerard@ensam.eu (S. Guérard).
[1] On leave from Université de Toulouse; INSA, UPS, Mines Albi, ISAE; ICA (Institut Clément Ader); 133, Avenue de Rangueil, F-31077 Toulouse, France.

with micro-MRI. The aim of the study is to show the feasibility of the technique, and to evaluate measurement uncertainties in order to assess displacements in a compression test of cancellous bone taken from bovine femoral head.

2. Materials and methods

2.1. Specimen preparation

A (16 mm long, 100 mm^2 cross-section) parallelepiped was extracted from a frozen bovine femoral head; its axis was parallel to that of the femoral neck. The dimensions were limited by the MRI antenna and the achievable field of view, which was 40 mm × 20 mm × 20 mm. A 20 mm thick slice was first cut with a band saw, perpendicular to the axis of the femoral neck. Then, the parallelepiped was extracted from this slice with a diamond saw and kept frozen until the MR experiment is performed. The marrow could be kept intact inside the sample thus providing an MR signal from the trabecular cavities.

2.2. Compression device

A mini-compression jig (Fig. 1) was built from a glass fiber reinforced PEEK (polyethyletherketone) to be MRI-compatible. The specimen was held in a threaded pipe (wall thickness of 2 mm) between two compression platen, a calibrated washer (acting as a load cell, which is not used herein) and two outer screws. It was glued with cyanoacrylate to one surface of the platen to place it at the center of the device without touching the inner wall. The container was entirely filled with water so that the washer load cell deformation could be monitored. A silicone cap was encapsulated around the lower end of the pipe to make it watertight. The load was prescribed by rotating the screw in contact with the washer so that the ball joint between the platen and the washer limited the rotation of the specimen with the screw. Two steps of loading were applied corresponding to a translation of the screw equal to 0.25 and 0.5 mm. The tested specimen was allowed to relax 20 min prior to image acquisition, so that the specimen reaches an equilibrium stress (as suggested by many studies from the literatures (Nazarian and Muller, 2004; Nagaraja et al., 2005; Thurner et al., 2006).

The compression device was put in the MRI coil. Its position was reproducible thanks to markers indicating the position in rotation and translation of the device inside the coil. The uncertainty of the positioning was about $\pm 5^\circ$ in rotation and ± 0.5 mm in translation. The translation has been easily calculated as a rigid body motion thanks to the correlation algorithm, but the images had to be rotated in order to decrease the rotation gap.

2.3. Image acquisition (micro-MRI)

MRI was performed on a vertical 9.4 T magnet with a 3D SE sequence and the following parameters: FOV 40 mm × 20 mm × 20 mm, matrix 512 × 256 × 256 voxels, TE/TR 8/1000 ms, BW 120 kHz, scan time 9 h (RARE factor 2), to get an isotropic resolution of 78 μm per voxel. A (37 mm in diameter) birdcage coil provided by the manufacturer was used. It created a B_1 radio-frequency field uniform over a cylindrical region of dimensions of about 20 mm in diameter and 20 mm in height.

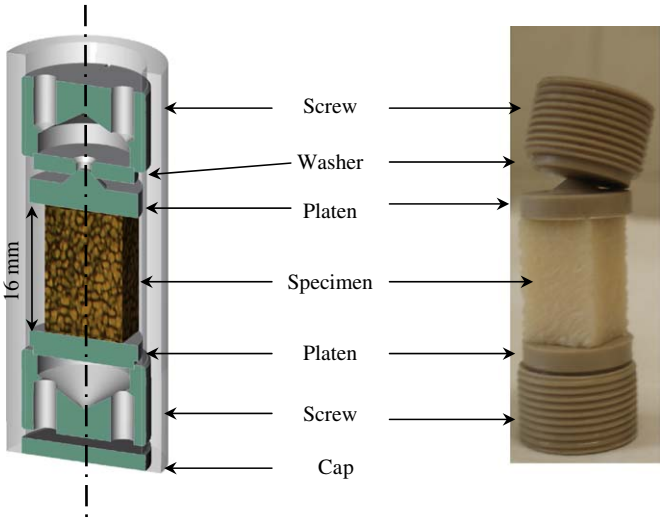

Fig. 1. Compression device.

The noise level of the 3D pictures was assessed in background areas in the images (out of signal areas). The noise distribution is known to follow a Rayleigh distribution, since MR images are obtained as the magnitude of a complex data set, after 3D Fourier transform of the measured signal. In signal areas, the signal distribution around the mean due to noise is expected to be Gaussian, with a standard deviation equal to the noise level n. The expected relationship between the mean m and the standard deviation σ_n in the noise areas ($m = \sigma_n\sqrt{(\pi/2)(2-\pi/2)}$), see Gudbjartsson and Patz (1995) was confirmed, and the noise level n was computed as

$$n = \frac{\sigma_n}{\sqrt{(2-\pi/2)}} \tag{1}$$

2.4. Displacement measurement by image correlation

An in-house 'finite-element based' digital image correlation software was used (Roux et al., 2008) to measure displacement fields. The spirit is to register as well as possible two gray level volumes, a first one, $f(\mathbf{x})$, called reference image, which corresponds to the unloaded stage, and a second one, $g(\mathbf{x})$, called deformed image, under load by using displacement bases associated with finite-element discretizations. They are assumed to be related through the brightness conservation hypothesis

$$g(\mathbf{x}) = f(\mathbf{x} + \mathbf{u}(\mathbf{x})) \tag{2}$$

The displacement field, $\mathbf{u}(\mathbf{x})$, is decomposed over a set of finite-element shape functions $\mathbf{u}(\mathbf{x}) = \Sigma a_n \boldsymbol{\varphi}_n(\mathbf{x})$. Here 8-node cubic elements with polynomial functions of order 1 (C8-P1) are used. A weak form of the brightness conservation (Galerkin approach) is implemented through the minimization of the domain integral over the whole considered domain of the quadratic difference $r^2(\mathbf{x}) = [g(\mathbf{x}) - f(\mathbf{x}+\mathbf{u}(\mathbf{x}))]^2$. After an initial rigid body translation correction, a multiscale linearization procedure allowing for good convergence properties is used. Details on the algorithm can be found in Roux et al. (2008). This implementation is a major difference with "local" approaches (Bay et al., 1999), or such as the ones compared in Liu and Morgan (2007) that consist in registering *small and independent* volumes.

2.5. A priori performances

To give confidence in the following results, a performance analysis is first performed. The performance of the correlation depends on the quality of the texture of the images to be analyzed. An image that has large gradients, with an almost random texture will be a good choice. Hence, the uncertainty of the displacement measurement is first assessed *a priori* on the reference image, when the specimen is not loaded. This was performed over a volume of 96 × 96 × 96 voxels or 7.5 mm × 7.5 mm × 7.5 mm. An artificial displacement of 0.5 voxel in each direction is artificially prescribed to the volume, creating a new (and artificially) "deformed" image. This displacement corresponds to a critical situation where the information contained in the reference and deformed images is the most biased (Roux et al., 2008). Then, the two images are registered and the artificial translation is subtracted from the measured displacement. The mean error thus corresponds to the average of the difference between the measured and prescribed displacements, and the standard uncertainty to the corresponding standard deviation.

To assess *a posteriori* the quality of the displacement measurement a distance criterion (or dimensionless correlation residual) between the two images f and g is used

$$R = \frac{\langle |r| \rangle}{\max(f) - \min(f)} \tag{3}$$

where $\langle \cdot \rangle$ is the average value over the considered ROI, $\max(\cdot)$ and $\min(\cdot)$ are the maximum and minimum values of the gray levels present in the image. This dimensionless indicator is equal to 0 when the two images are identical, or when no correlation error occurs.

2.6. Strain evaluations

From the measured displacement fields, the mean strain per element is assessed by using the C8 interpolation functions. Further, when the displacement field is interpolated over a gauge volume by using a single trilinear polynomial, macroscopic principal strains are assessed by using the mean transformation gradient.

3. Results

3.1. A priori performances

Fig. 2 shows the mean displacement error and the standard uncertainty as functions of the element size used for the volume correlation calculation. The mean error is always less than the standard uncertainty, the results of the correlation were therefore considered as unbiased. Its level is very low, and is independent of the element size. Moreover the standard displacement uncertainty decreases when the element size increases. From these values, it is concluded that the displacements are assessed with subvoxel resolution.

Strain uncertainties are also evaluated by using the previously measured displacement field. Very small standard uncertainties are obtained yielding strain resolutions less than 3×10^{-2} for element sizes greater than or equal to 12 voxels.

3.2. Displacement measurement

The quality of the displacement measurement is analyzed for both loading steps on a region of interest (ROI) of $96 \times 192 \times 96$ voxels (or $7.5\,\text{mm} \times 15\,\text{mm} \times 7.5\,\text{mm}$). The initial value of R between the reference image and the image of the specimen after the first loading step is equal to 11.3% when only the ROI was considered. As a starting point, rigid body translations (corresponding to an isometric transformation) are corrected for, and this leads to a reduction of R to 4.2%. With optical images of good quality, the correlation algorithm enables one to reach a final value of about 1% (Besnard et al., 2006). In the present case, the correlation residuals are about 1.4% for the first step of loading with an element size of 12 voxels at the end of the correlation procedure. For the second loading step, the initial value of R is 10.8%. After the removal of rigid body translation, it reduces to 5.7%, and after convergence it reached 1.6% for 12-voxel elements.

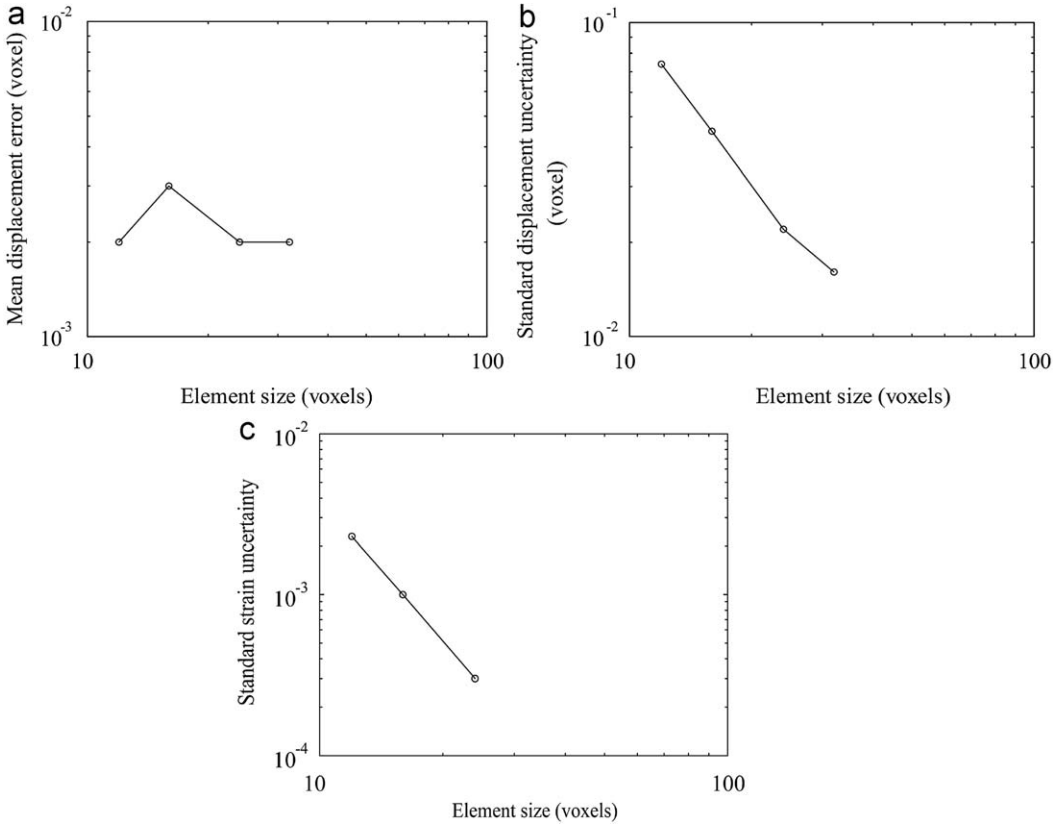

Fig. 2. Mean error (a), standard uncertainty (b) of the displacement measurement and standard strain uncertainty (c) as functions of the element size.

Table 1
Influence of the element size for the first (a) and the second (b) loading steps on various parameters: mean displacement, correlation residual, minimum principal strain.

Element size (voxels)	$\langle u_x \rangle$ (voxels)	$\langle u_y \rangle$ (voxels)	$\langle u_z \rangle$ (voxels)	Residual (%)	$\langle \varepsilon_1 \rangle$ (%)
(a)					
12	−4.68	−9.82	−6.62	1.4	−0.6
16	−4.70	−9.81	−6.61	1.4	−0.6
24	−4.68	−9.81	−6.62	1.5	−0.5
32	−4.67	−9.81	−6.62	1.7	−0.5
(b)					
12	−11.81	4.53	−20.63	1.6	−1.0
16	−11.80	4.54	−20.63	1.7	−1.0
24	−11.79	4.55	−20.64	1.9	−0.9
32	−11.78	4.55	−20.64	2.2	−0.9

The quality of the correlation was very satisfactory although it varied slightly with the element size. Table 1 summarizes the final gaps as functions of the element size.

The residual maps (Fig. 4) show that correlation residuals are not only very small on average, but also locally for the two loading steps. The gray level histograms of Fig. 4 can be compared to that of the reference picture (Fig. 3). The residual level is very small. Furthermore, the standard deviation of the residual can be compared to the noise level that was estimated. The noise level is about 2.4 gray levels when the image data is limited to an 8-bit range. It changes by less than 10% along the long specimen axis (also the probe axis) over the region of interest. From the standard deviation of the correlation residual (respectively equal to 4 and 4.3 gray levels), the standard deviation associated with each volume is equal to the former divided by $\sqrt{2}$ (namely, 2.8 and 3 gray levels). The two values are very close to the noise level. The measurement results are therefore deemed trustworthy.

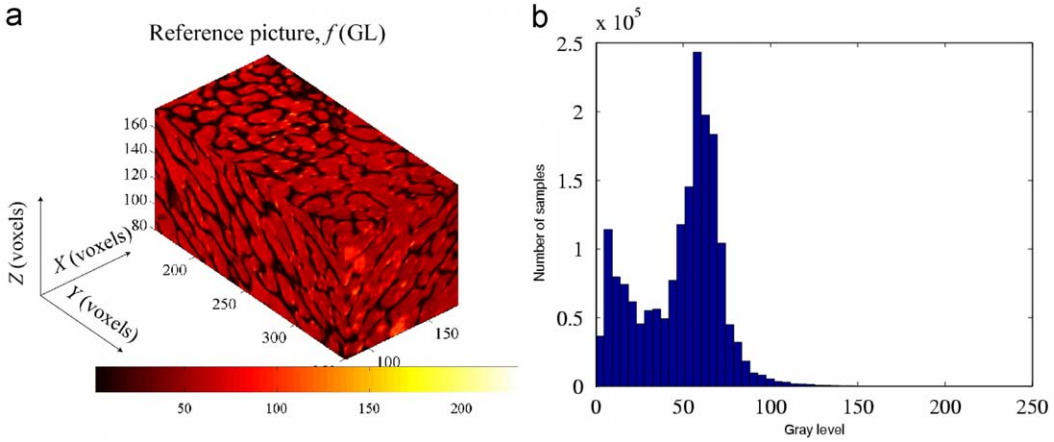

Fig. 3. Reference region of interest (a) in gray levels (size: 96 × 192 × 96 voxels or 7.5 mm × 15 mm × 7.5 mm) and corresponding histogram of gray levels (b) (dynamic range: 8 bits).

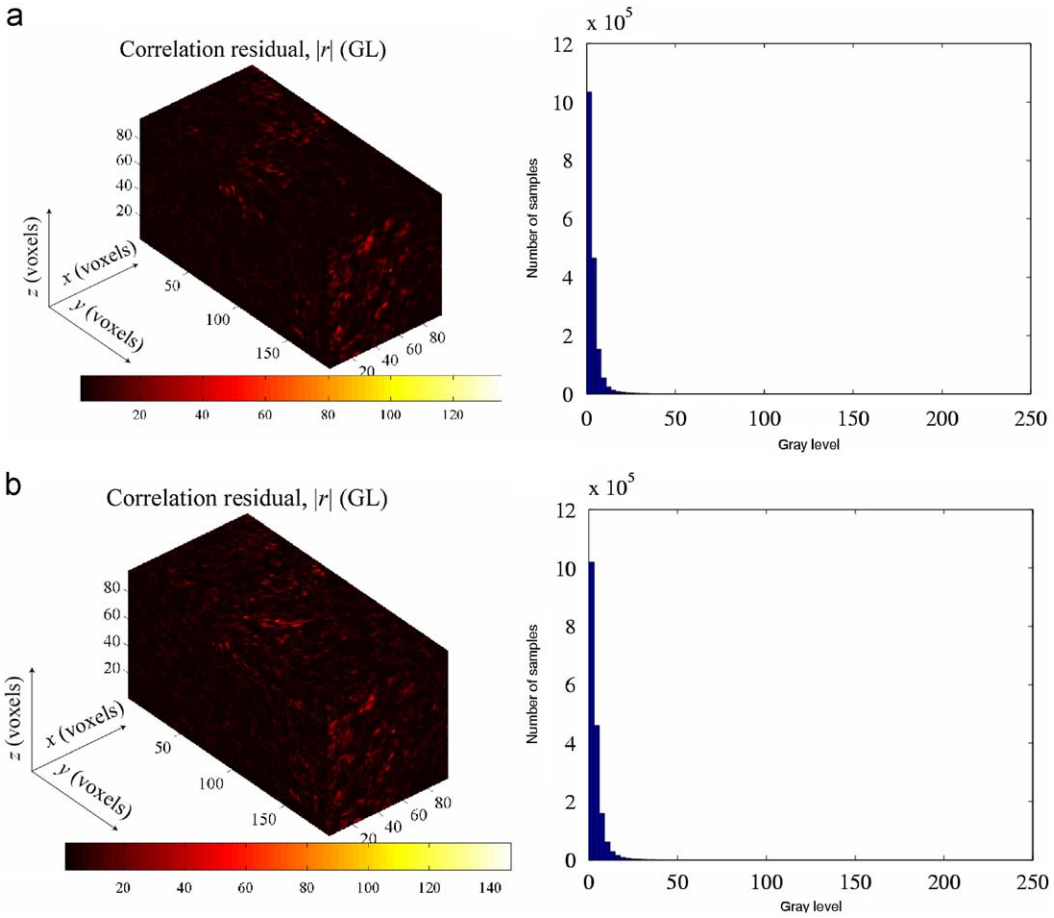

Fig. 4. Correlation residual measured in gray levels and corresponding histogram with the same dynamic range as Fig. 3(b) for a ROI of 96 × 192 × 96 voxels and an element size of 12 voxels, for the first loading step (a) and for the second loading step (b).

3.3. Strain fields

In the present case, the mean strain levels per element are determined by using the (trilinear) interpolation functions associated with the discretization. The values of the latter are assigned to the center of the element, and linearly interpolated between these points to obtain 3D maps whose cuts by two perpendicular planes containing the longitudinal axis of the ROI are shown in Fig. 5 for the two load levels when 12-voxel elements are used. The strain field is not uniform for the first and second load levels.

To quantify this result even more, a gauge volume of size $96 \times 96 \times 96$ voxels (or $7.5\,\text{mm} \times 7.5\,\text{mm} \times 7.5\,\text{mm}$) is moved along the specimen axis by increments equal to the element size. The displacement field is interpolated trilinearly and the mean transformation gradient estimated. The nominal strain tensor is computed and its eigen values extracted. The change of the three eigen strains is shown in Fig. 6 for the two load levels for 12-voxel elements. As one moves from the top to the bottom of the longitudinal axis, it is observed that the mean strain state varies significantly. When compared to the previous results, the use of 16, 24 and 32-voxel elements in the gauge volume changes the results by $\pm 2 \times 10^{-4}$ at most.

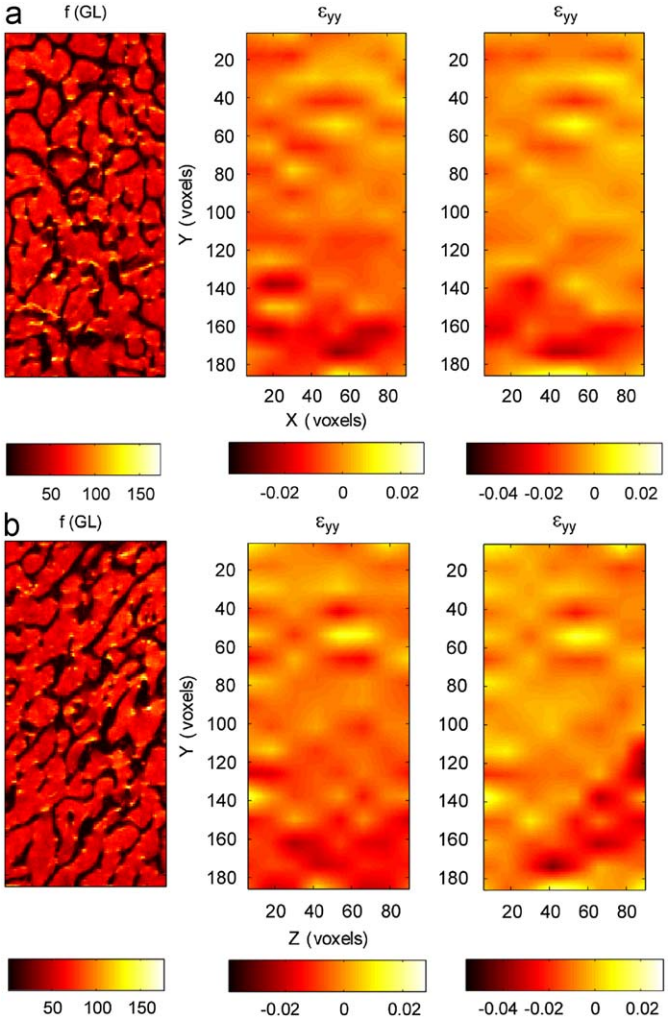

Fig. 5. Cuts along two planes containing the longitudinal axis of the region of interest. The gray level picture and the longitudinal strain fields corresponding to the two loading steps are shown.

4. Discussion

This article presents a mechanical compression device and a three-dimensional DIC technique that uses micro-MRI images of bovine cancellous bone that allows for the measurement of displacement and strain fields. The overall aim of this study is to demonstrate the feasibility of using 3D digital image correlation on compressed bovine cancellous bone monitored by micro-MRI.

The standard displacement and strain uncertainties decrease when the element size increases. This result is explained by the fact that there are more data (voxels) in large size elements to make the correlation between the reference and deformed images more secure. However, if the element size is too large, the number of measurement points in the specimen will be limited and the displacement will be prone to interpolation errors, in particular in the presence of localized phenomena.

The map and histogram of correlation residuals (Fig. 4) show that the errors are very small, and very close to the noise levels due to the acquisition device. This result fully validates not only the *a priori* analysis on artificial displacement, but also the whole experimental procedure developed to measure accurately displacement fields when using MRI.

From the measured strain fields, it is concluded that for the two analyzed load levels, no uniformity is achieved in terms of mesoscopic strains (i.e., on the scale of each finite element), and macroscopic strains (i.e., at the level of the gauge volume). This phenomenon is related to the coarse microstructure (at the scale of micro-MRI) of trabecular bone. Even though a compressive load is applied, the material response is not that expected from a

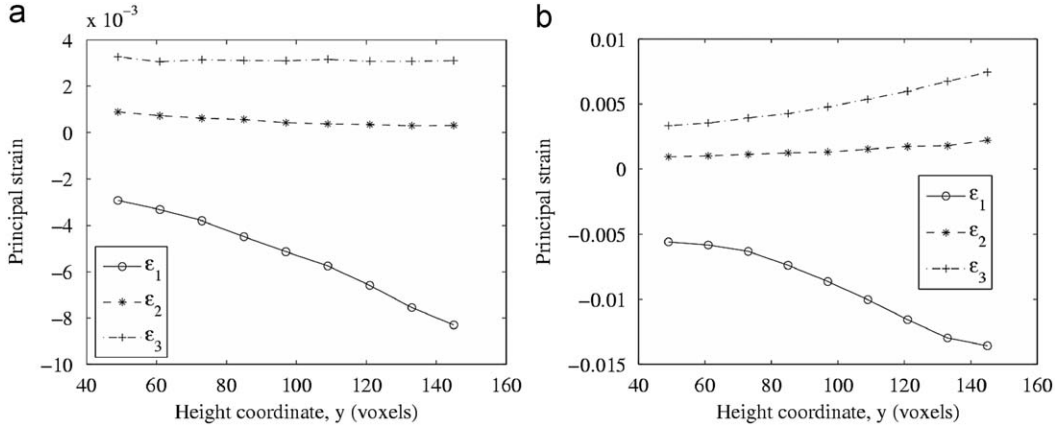

Fig. 6. Macroscopic principal strains as functions of the longitudinal position of the gauge volume for the first loading step (a) and for the second loading step (b).

homogeneous medium. This observation shows that even if elasticity can be assumed (since the first mean strain level is equal to 0.6%), the elastic properties (e.g., Poisson's ratio) cannot be inferred from the present observations. This is not a drawback of the experimental procedure, or of the measurement technique, but an effect of the microstructure at hand. This result shows that more advanced identification procedures are called for to evaluate the microscopic properties.

5. Conclusion

Volume correlation was used on a loaded bovine cancellous bone monitored by micro-MRI leading to 3D-displacement fields of subvoxel uncertainty less than 0.1 voxel (or 8 μm) for element sizes greater than 12 voxels. The mean correlation residuals remain less than 1.4% of the image dynamic range for 12-voxel elements, and the displacement fields were stable for each tested element size. The corresponding standard deviation is very close to the noise level, thereby proving that the registration was successful, and the measured displacements are trustworthy.

From the measured displacements, macroscopic and mesoscopic strain fields were evaluated. The latter show that the local strain field is not uniform in the present experiment. This phenomenon is due to the coarseness of the studied microstructure. Furthermore, the variation of the macroscopic principal strains along the height of the sample shows that a classical identification procedure to evaluate Poisson's ratio would lead to erroneous results. More advanced identification tools are needed to determine the elastic parameters at a microscopic (at the level of trabeculae), mesoscopic (at the level of the elements considered herein) or even macroscopic scale (i.e., the studied sample). This analysis shows that the representative volume element is significantly larger than the volume tested herein. Such methodology opens the way for in-depth validation of micro-finite-element models of cancellous bone.

Last, MRI has a wide field of application to other types of biological tissues. By means of some adaptations, it could be possible to measure macroscopic damage on soft tissues such as cartilages or ligaments.

Conflict of interest

There are no conflicts of interest related to the work submitted in this manuscript.

Acknowledgement

The authors would like to acknowledge Claude Verliac and Joachim Magnier for technical advice on the manufacturing process of the mechanical loading system.

References

Bay, B.K., Yerby, S.A., McLain, R.F., Toh, E., 1999. Measurement of strain distributions within vertebral body sections by texture correlation. Spine 24, 10–17.

Besnard, G., Hild, F., Roux, S., 2006. Finite-element displacement fields analysis from digital images: application to portevin-le châtelier bands. Exp. Mech. 46, 789–803.

Carter, D.R., Hayes, W.C., 1976. Bone compressive strength: the influence of density and strain rate. Science 194, 1174–1176.

Duchemin, L., Bousson, V., Raossanaly, C., Bergot, C., Laredo, J.D., Skalli, W., Mitton, D., 2008. Prediction of mechanical properties of cortical bone by quantitative computed tomography. Med. Eng. Phys. 30, 321–328.

Glaser, K.J., Felmlee, J.P., Manduca, A., Kannan Mariappan, Y., Ehman, R.L., 2006. Stiffness-weighted magnetic resonance imaging. Magn. Reson. Med. 55, 59–67.

Gudbjartsson, H., Patz, S., 1995. The Rician distribution of noisy MRI data. Magn. Reson. Med. 34, 910–914.

Hollister, S.J., Brennan, J.M., Kikuchi, N., 1994. A homogenization sampling procedure for calculating trabecular bone effective stiffness and tissue level stress. J. Biomech. 27, 433–444.

Liu, L., Morgan, E.F., 2007. Accuracy and precision of digital volume correlation in quantifying displacements and strains in trabecular bone. J. Biomech. 40, 3516–3520.

Mosekilde, L., 1988. Age-related changes in vertebral trabecular bone architecture—assessed by a new method. Bone 9, 247–250.

Nagaraja, S., Couse, T.L., Guldberg, R.E., 2005. Trabecular bone microdamage and microstructural stresses under uniaxial compression. J. Biomech. 38, 707.

Nazarian, A., Muller, R., 2004. Time-lapsed microstructural imaging of bone failure behavior. J. Biomech. 37, 55–65.

Neu, C.P., Walton, J.H., 2008. Displacement encoding for the measurement of cartilage deformation. Magn. Reson. Med. 59, 149–155.

Nicolella, D.P., Nicholls, A.E., Lankford, J., Davy, D.T., 2001. Machine vision photogrammetry: a technique for measurement of microstructural strain in cortical bone. J. Biomech. 34, 135.

Parfitt, A.M., 1987. Trabecular bone architecture in the pathogenesis and prevention of fracture. Am. J. Med. 82, 68–72.

Rice, J.C., Cowin, S.C., Bowman, J.A., 1988. On the dependence of the elasticity and strength of cancellous bone on apparent density. J. Biomech. 21, 155–168.

Roux, S., Hild, F., Viot, P., Bernard, D., 2008. Three-dimensional image correlation from X-ray computed tomography of solid foam. Compos. Part A: Appl. Sci. Manuf. 39, 1253.

Thurner, P.J., Wyss, P., Voide, R., Stauber, M., Stampanoni, M., Sennhauser, U., Müller, R., 2006. Time-lapsed investigation of three-dimensional failure and damage accumulation in trabecular bone using synchrotron light. Bone 39, 289.

van Rietbergen, B., Weinans, H., Huiskes, R., Odgaard, A., 1995. A new method to determine trabecular bone elastic properties and loading using micromechanical finite-element models. J. Biomech. 28, 69–81.

Verhulp, E., van Rietbergen, B., Huiskes, R., 2004. A three-dimensional digital image correlation technique for strain measurements in microstructures. J. Biomech. 37, 1313–1320.

Zauel, R., Yeni, Y.N., Bay, B.K., Dong, X.N., Fyhrie, D.P., 2006. Comparison of the linear finite element prediction of deformation and strain of human cancellous bone to 3D digital volume correlation measurements. J. Biomech. Eng. 128, 1–6.